ELSEVIER

Modeling the optical properties of WO_3 and WO_3–SiO_2 thin films

D. Saygin-Hinczewski[a,1], M. Hinczewski[b,1], I. Sorar[a], F.Z. Tepehan[a], G.G. Tepehan[c,*]

[a]*Department of Physics, Istanbul Technical University, Maslak 34469, Istanbul, Turkey*
[b]*Feza Gürsey Research Institute, TÜBİTAK–Bosphorus University, Çengelköy 34680, Istanbul, Turkey*
[c]*Faculty of Arts and Sciences, Kadir Has University, Cibali 34083, Istanbul, Turkey*

Abstract

The optical properties and surface morphology of sol–gel spin coated WO_3 and WO_3–SiO_2 composite films annealed at 250 and $400\,^{\circ}C$ are investigated. For the purpose of extracting the optical parameters of the films, a novel form for the dielectric function is introduced, consisting of two Tauc–Lorentz oscillators and an Urbach tail component, which is suited for amorphous multi-transition materials with substantial subgap absorption. The evolution of the refractive indices, transmittances, and band gaps with doping is marked by sizable shifts at 2.0–2.5% SiO_2 doping for the $250\,^{\circ}C$ films, and 4.0–4.5% doping for the $400\,^{\circ}C$ films. In addition, pronounced changes in the surface roughness of the films occur at these doping values.
© 2008 Elsevier B.V. All rights reserved.

Keywords: Sol–gel; WO_3; WO_3–SiO_2; Double Tauc–Lorentz model; Urbach tail; Optical properties; Surface morphology

1. Introduction

Tungsten oxide films have a wide variety of potential uses, among them electrochromic [1–5], photochromic [2,6], gasochromic [2,7], and gas sensing applications [8]. Composite materials containing WO_3 offer the opportunity for enhanced behavior compared to the pure films. In the context of electrochromism, research has focused on increasing coloration efficiency, improving durability, and obtaining faster reaction kinetics. In the particular case of WO_3–SiO_2 films, electrochromic coloration ability persists up to a moderate doping of SiO_2 [9], and they can exhibit high coloration densities and fast response times [10]. WO_3–SiO_2 composites have also shown promising results in other areas. Compared to pure WO_3, the films exhibit higher sensitivity to NO_2, making them good candidates for environmental nitrogen detector applications [11], and have a faster coloration rate in gasochromic smart windows [12]. At a particular concentration (15 mol% SiO_2) these films are known to exhibit superhydrophilic surfaces without UV or visible irradiation [13]. WO_3–SiO_2 materials were also investigated as catalysts [14–17].

The present study fills a gap in the earlier research, by examining in detail the evolution of the optical properties and the surface morphology of WO_3–SiO_2 thin films with SiO_2 doping. The films were prepared through the sol–gel spin coating method, for SiO_2 dopings up to 5 mol%. To facilitate the analysis, we constructed a dielectric model incorporating the main features which determine the optical response of the films in the near-UV and visible region: two interband transitions for energies $E \gtrsim 3\,eV$, and as the films are amorphous, an exponential (Urbach) absorption tail in the subgap part of the spectrum. The resulting model, a novel combination of two Tauc–Lorentz (TL) [18] oscillators together with an Urbach tail component [19], works equally well for pure WO_3 films as for the composites, and has the potential to be applied to any material where multi-transition and Urbach tail effects are significant.

2. Experimental procedure

Corning 2947 substrates were first rinsed with water and then washed with laboratory detergent. They were flushed

---

*Corresponding author.
E-mail address: tepehan@khas.edu.tr (G.G. Tepehan).
[1]These authors have contributed equally to this work.

off with tap water, put in a beaker full of ethanol and placed in an ultrasonic bath for 15 min. Five grams of tungsten hexachloride (Aldrich, 99.9 + %, WCl_6) was stirred with 50 ml of ethanol (Merck, 99.9%, C_2H_5OH) to form the tungsten oxide solution. An amount of 0.669 ml tetraethoxysilane (Sigma-Aldrich, 99.999%, $Si(OC_2H_5)_4$) was stirred with 5.3 ml of ethanol, 1.69 ml of distilled water, and 0.24 ml of hydrochloric acid (Merck, 37%, HCl) for half an hour to get the SiO_2 solution. Both of the solutions were prepared in air at room temperature. The final solutions were mixed for 10 min in mole ratios $(100 - x)\% WO_3 - x\% \ SiO_2$, with $x = 0, 0.5, 1, \ldots, 5$. The solutions were then immediately coated on the substrates using a spin coater with 2000 rpm for 10 s. All the films were pre-annealed in a furnace operating at 100 °C for half an hour. Samples were prepared for two different annealing temperatures, 250 and 400 °C, in each case rising from 100 °C with a ramp up of 3 °C/min, held at the final temperature for 1 h, and then left in the furnace to cool down. The reflectance and transmittance of the film–substrate systems were measured with a spectrophotometer (NKD 7000, Aquila, UK) at an incident angle of 30° over the spectral range 300–1000 nm. Surface morphology was investigated through an atomic force microscope (AFM, SPM-9500J3, Shimadzu) in contact mode. Crystal structure analysis was performed using an X-ray diffractometer (GBC-MMA) with CuK_α radiation. The step size was chosen as $0.05° \ (2\theta)/s$ for the scan from 10° to 60° (2θ). All the measurements above were conducted over several days following the coating.

3. Theoretical model

The measured transmittance $T(\lambda)$ and reflectance $R(\lambda)$ of the film–substrate system can be related to the optical properties of the film alone with an approach similar to the ones described in Refs. [20,21]. We used a three-layer model consisting of the substrate—characterized by thickness d_{sub}, refractive index $n_{sub}(\lambda)$, and absorption coefficient $\alpha_{sub}(\lambda)$—the film, with analogous parameters d, $n(\lambda)$, $\alpha(\lambda)$, and an overlayer of thickness d_{rough} consisting of 50% material, 50% voids [22] to model the surface roughness of the film. The optical characteristics of this overlayer were related to dielectric function of the film through the Bruggeman effective medium approximation [23]. The substrate optical functions were determined directly from reflectance and transmittance spectra of the uncoated substrate, and the resulting $n_{sub}(\lambda)$ and intensity attenuation factor $\delta_{sub}(\lambda) = \exp(-\alpha_{sub}(\lambda)d_{sub})$ are shown in Ref. [21]. Through $\delta_{sub}(\lambda)$ the model takes into account the loss of intensity for reflected or transmitted beams passing through the substrate, which is significant in the near-UV region $(\lambda \lesssim 350 \, \text{nm})$.

To model the film optical parameters $n(\lambda)$ and $\alpha(\lambda)$, we chose a form for the dielectric function which allows for three key aspects of optical absorption in the amorphous WO_3 and WO_3–SiO_2 composite thin films

under consideration: at low energies ($\lesssim 3 \, \text{eV}$) there is an exponential Urbach tail; in the near-UV range (~ 2.9–$3.6 \, \text{eV}$) the absorption edge has the form of the Tauc law [24]; finally, at slightly higher energies (~ 3.7–$4.1 \, \text{eV}$), the absorption behavior changes, scaling like a direct transition. All three of these have been observed for pure amorphous WO_3 [25], and as we will see below, these features persist throughout the SiO_2 doping range which we examined. We found that the different absorption regimes could be captured by a dielectric function involving two interband transitions: one of the transitions is modeled through a TL oscillator [18], while the other transition and the subgap absorption are described through a modified version of the TL oscillator which incorporates the Urbach tail (the TLU model) [19]. In recent years TL functions have found widespread application in a variety of contexts, from semiconductors to dielectric optical coating materials [26,27]. Their success stems from two characteristics: (1) the imaginary part of the TL dielectric function is a product of a Tauc law term and a Lorentz oscillator, thus approximately accounting for the optical properties of the material both near the band gap and at larger energies; (2) the real and imaginary parts of the TL dielectric function correctly satisfy the Kramers–Kronig transformation, a feature which is absent in many earlier models. These properties allow the TL function to accurately reflect experimental results over a wide spectral range. Two TL oscillators have been combined in the past to describe multi-transition materials [28,29], but to our knowledge the present study is the first application of a double TL model incorporating Urbach tail effects (which we will call the DTLU model).

The imaginary part of the DTLU dielectric function $\varepsilon_2(E)$ as a function of photon energy E is given by a sum of the TL and TLU contributions:

$$\varepsilon_2(E) = \varepsilon_{2TL}(E) + \varepsilon_{2TLU}(E). \tag{1}$$

The TL term has the form [18]:

$$\varepsilon_{2TL}(E) = \begin{cases} \dfrac{A_1 E_{01} \Gamma_1 (E - E_{g1})^2}{E[(E^2 - E_{01}^2)^2 + \Gamma_1^2 E^2]} & \text{for } E > E_{g1}, \\ 0 & \text{for } E \leqslant E_{g1}. \end{cases} \tag{2}$$

Here there are four fitting parameters with the dimension of energy, defined as follows: E_{g1} is the band gap and A_1, E_{01}, and Γ_1 are the Lorentz oscillator amplitude, resonance energy, and oscillator width, respectively. The TLU term has a similar form, but with the addition of an Urbach tail component at lower energies [19]:

$$\varepsilon_{2TLU}(E) = \begin{cases} \dfrac{A_2 E_{02} \Gamma_2 (E - E_{g2})^2}{E[(E^2 - E_{02}^2)^2 + \Gamma_2^2 E^2]} & \text{for } E > E_t, \\ \dfrac{E_c}{E} \exp\left(\dfrac{E - E_t}{E_u}\right) & \text{for } E \leqslant E_t. \end{cases} \tag{3}$$

The parameters E_{g2}, A_2, E_{02}, and Γ_2 have the same roles as in the TL term, and there are two additional variables: E_t

marks the border between the region of Urbach tail and interband transitions, with $E_t \geqslant E_{g2}$; E_u controls the width of the Urbach tail. The $E \geqslant E_t$ part of ε_{2TLU} yields a subgap absorption coefficient $\alpha(E) \propto \exp(E/E_u)$. The parameter E_c is not free, but chosen so that $\varepsilon_{2TLU}(E)$ is continuous at $E = E_t$. Likewise we can impose the constraint that the slope of $\varepsilon_2(E)$ be continuous at $E = E_t$, which is approximately satisfied by fixing $E_t = E_{g2} + 2E_u$ [19]. This leaves five free parameters specifying the TLU term: E_{g2}, A_2, E_{02}, Γ_2, and E_u.

The real part of the DTLU dielectric function $\varepsilon_1(E)$ is calculated through the Kramers–Kronig integral:

$$\varepsilon_1(E) = \varepsilon_{1\infty} + \frac{2}{\pi} P \int_0^\infty d\xi \frac{\xi \varepsilon_2(\xi)}{\xi^2 - E^2}, \qquad (4)$$

where the integration variable ξ runs over the entire energy range, P denotes the Cauchy principal value of the integral, and $\varepsilon_{1\infty}$ is an additional parameter, which can be fixed by physical constraint to $\varepsilon_{1\infty} = 1$ [19].

The complex dielectric function $\varepsilon_{rough}(E)$ of the surface roughness layer is related to the complex dielectric function $\varepsilon(E) = \varepsilon_1(E) + i\varepsilon_2(E)$ of the film through the following equation:

$$\frac{1}{2}\left(\frac{1 - \varepsilon_{rough}}{1 + 2\varepsilon_{rough}}\right) + \frac{1}{2}\left(\frac{\varepsilon - \varepsilon_{rough}}{\varepsilon + 2\varepsilon_{rough}}\right) = 0 \qquad (5)$$

derived from the Bruggeman effective medium approximation [23], with 50% voids, 50% material. Thus with the overlayer thickness d_{rough} and the film thickness d, we have a total of 11 free parameters in the DTLU model.

The film refractive index n and absorption coefficient α are related to ε_1 and ε_2 as

$$n = \left[\frac{(\varepsilon_1^2 + \varepsilon_2^2)^{1/2} + \varepsilon_1}{2}\right]^{1/2},$$

$$\alpha = \frac{2E}{\hbar c}\left[\frac{(\varepsilon_1^2 + \varepsilon_2^2)^{1/2} - \varepsilon_1}{2}\right]^{1/2}. \qquad (6)$$

Through the dependence of $R(\lambda)$ and $T(\lambda)$ for the film–substrate system on the film optical functions $n(\lambda)$ and $\alpha(\lambda)$, we can vary the 11 free parameters of the DTLU model and perform a least squares fit of the experimental $R(\lambda)$ and $T(\lambda)$ data. This is done using the Levenberg–Marquardt multivariate-regression algorithm, implemented through the MINPACK library [30].

To illustrate why the full complexity of the DTLU model is necessary to accurately represent the optical properties of $(100 - x\%)$ WO$_3$–$x\%$ SiO$_2$ films, Fig. 1 shows a comparison between the DTLU model and a simpler form for the dielectric function: a single TLU oscillator with seven free parameters (including d and d_{rough}), which incorporates only one interband transition. Results for two samples are shown, at $x = 0\%$ and 5%, both annealed at 400 °C. In the top panels, it is seen that both the DTLU and TLU models give reasonable best-fits to the measured R and T data of the film–substrate system. However they give quite

different results for the film thickness: the DTLU model yields $d(x = 0\%) = 38$ nm, $d_{rough}(x = 0\%) = 21$ nm, and $d(x = 5\%) = 50$ nm, $d_{rough}(x = 5\%) = 0$ nm, while the TLU model gives $d(x = 0\%) = 73$ nm, $d_{rough}(x = 0\%) = 9$ nm, and $d(x = 5\%) = 98$ nm, $d_{rough}(x = 5\%) = 0$ nm. To check the consistency of the models more thoroughly, we can use the best-fit thicknesses d and d_{rough} to numerically invert the R and T experimental data, giving directly the real and imaginary parts of the dielectric function $\varepsilon_1(E)$ and $\varepsilon_2(E)$. These are plotted in the center and bottom panels of Fig. 1, along with the DTLU and TLU results for the dielectric function. The DTLU curve closely reproduces the inversion data throughout the entire measured spectrum. In particular for ε_2 it accurately captures both the onset of the absorption in the near-UV region and the shape of the subgap tail. For the TLU model, on the other hand, there are significant discrepancies at higher energies, $E \gtrsim 3$ eV. This is a clear indication that a single TLU oscillator is insufficient to fully describe the optical response of the material, making the TLU best-fit results unreliable. We have found that for all film compositions in the study, the DTLU model provides a superior representation of the film dielectric function.

Selected DTLU best-fit parameters for films of various compositions and annealing temperatures are listed in Tables 1 and 2. For all the cases, the dominant contribution to the dielectric function is the TLU oscillator, with an amplitude $A_2 \sim 120-170$ eV, and a bandgap value $E_{g2} \sim 3.3-3.7$ eV (for the 250 °C films), ~ 4 eV (for the 400 °C films). The TL oscillator provides a smaller component, with amplitude $A_1 \sim 10-50$ eV, typically with a bandgap E_{g1} somewhat lower than the TLU one: $E_{g1} \sim 3.3-3.5$ eV (for the 250 °C films), $\sim 3.5-3.7$ eV (for the 400 °C films). Since the TL and TLU oscillators are only approximations to the true dielectric function, the nominal bandgaps E_{g1} and E_{g2} must be interpreted as fitting parameters which only roughly correspond to physical band gaps [19,26,29]. To get a better estimate of true gap values, we can look directly at the behavior of $\alpha(E)$ for energies just above the onset of absorption. We find $(E\alpha(E))^{1/2} \propto E - E_g^{Tauc}$ in the immediate vicinity of the absorption edge ($\sim 2.9-3.6$ eV), defining the so-called Tauc gap E_g^{Tauc} [24], a common feature of many amorphous materials. At slightly higher energies ($\sim 3.7-4.1$ eV) the scaling $(E\alpha(E))^2 \propto E - E_g^{dir}$ is a better fit, defining a second, larger gap value E_g^{dir}. Results for E_g^{Tauc} and E_g^{dir} are shown in Table 1. The latter gap is possibly related to the direct allowed transition between the 2p valence band of oxygen and the 5d conduction band of tungsten known to exist in crystalline and polycrystalline WO$_3$ in approximately the same energy range [25]. In this interpretation, the gap survives even in the absence of crystallinity, through the influence of the short-range ordering (deformed WO$_6$ octahedra in the amorphous material) on the electronic density of states. If this larger gap is a true mobility gap, between extended states in the valence band and extended states in the conduction band, then the
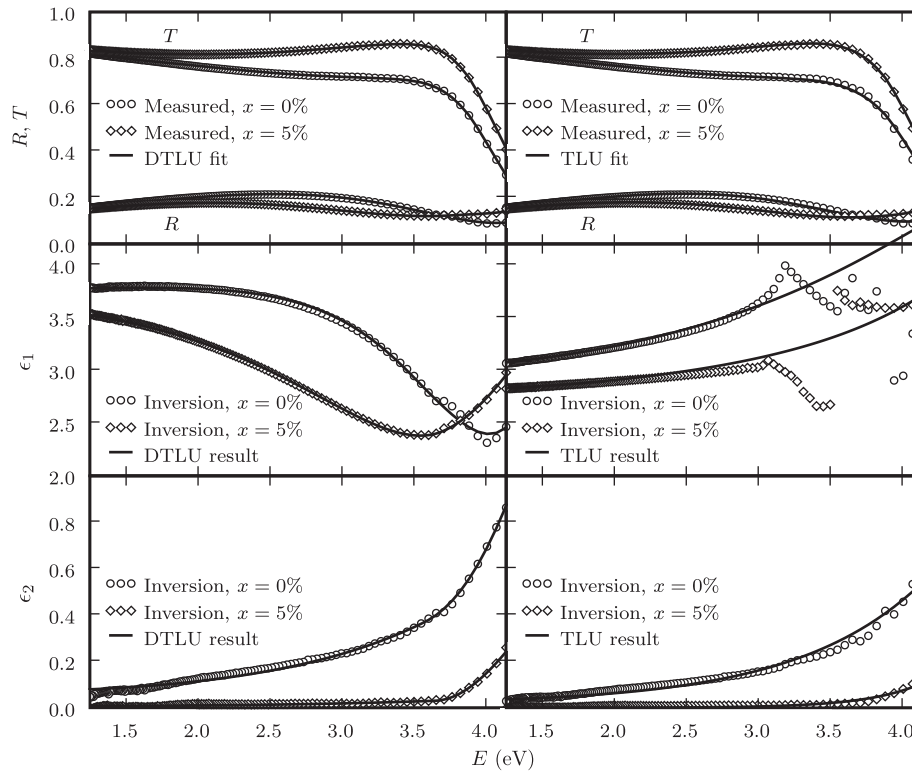
Fig. 1. Comparison of results from the DTLU model (left column) to those of the TLU model (right column) for $(100 - x)\%$ WO$_3$–$x\%$ SiO$_2$ films coated on a Corning 2947 substrate and annealed at 400 °C. Two compositions, $x = 0\%$ and 5%, are shown. The top panels plot the measured reflectance R and transmittance T of the film–substrate system as a function of photon energy E, along with the best-fit curves for the two models. The film thicknesses derived from the fitting are: $d(x = 0\%) = 38$ nm (DTLU), 73 nm (TLU); $d_{\text{rough}}(x = 0\%) = 21$ nm (DTLU), 9 nm (TLU); $d(x = 5\%) = 50$ nm (DTLU), 98 nm (TLU); $d_{\text{rough}}(x = 5\%) = 0$ nm (DTLU), 0 nm (TLU). Using these best-fit thicknesses, the real and imaginary parts of the film dielectric function $\varepsilon_1(E)$ and $\varepsilon_2(E)$ can be calculated by inverting the R and T data. These inversion results are shown in the center and bottom panels, together with $\varepsilon_1(E)$ and $\varepsilon_2(E)$ from the DTLU and TLU models. The DTLU model is everywhere consistent with the inversion results, whereas the TLU model diverges for $E \gtrsim 3$ eV, indicating that the TLU best-fit results are unreliable.

Table 1
Selected best-fit results of the DTLU model for $(100 - x)\%$ WO$_3$–$x\%$ SiO$_2$ films annealed at 250 and 400 °C

Temp. (°C)	$x\%$	A_1 (eV)	E_{g1} (eV)	A_2 (eV)	E_{g2} (eV)	E_u (eV)	E_g^{Tauc} (eV)	E_g^{dir} (eV)
250	0.0	26 ± 3	3.32 ± 0.02	125 ± 7	3.40 ± 0.02	0.81 ± 0.01	3.06 ± 0.01	3.75 ± 0.02
	2.0	30 ± 3	3.37 ± 0.02	163 ± 18	3.68 ± 0.02	0.80 ± 0.01	3.10 ± 0.01	3.78 ± 0.02
	2.5	25 ± 2	3.35 ± 0.01	142 ± 5	3.58 ± 0.02	0.80 ± 0.01	3.17 ± 0.01	3.81 ± 0.01
	4.0	26 ± 3	3.33 ± 0.01	155 ± 4	3.74 ± 0.02	0.84 ± 0.01	3.17 ± 0.01	3.81 ± 0.02
	4.5	30 ± 7	3.45 ± 0.03	123 ± 10	3.32 ± 0.02	0.83 ± 0.01	2.93 ± 0.02	3.72 ± 0.02
400	0.0	27 ± 5	3.57 ± 0.02	168 ± 27	4.07 ± 0.03	0.90 ± 0.01	3.08 ± 0.02	3.90 ± 0.04
	2.0	12 ± 1	3.50 ± 0.01	129 ± 3	4.00 ± 0.02	0.96 ± 0.01	3.32 ± 0.01	3.94 ± 0.02
	2.5	40 ± 6	3.63 ± 0.01	153 ± 14	3.96 ± 0.09	1.09 ± 0.02	3.54 ± 0.02	4.04 ± 0.01
	4.0	38 ± 5	3.61 ± 0.02	133 ± 6	4.28 ± 0.04	1.39 ± 0.02	3.47 ± 0.01	4.03 ± 0.01
	4.5	48 ± 15	3.71 ± 0.01	162 ± 18	3.95 ± 0.07	1.09 ± 0.02	3.59 ± 0.08	4.06 ± 0.01

The gap values E_g^{Tauc} and E_g^{dir} are obtained by linear extrapolation of $(E\alpha(E))^v$ with respect to E, with $v = 1/2$ for E_g^{Tauc}, and $v = 2$ for E_g^{dir}.

smaller Tauc gap which is also observed may arise from transitions involving localized states inside the mobility gap. (In amorphous WO$_3$ these localized states may exist both on the bottom of conduction band and on the top of the valence band [25].) The magnitude of absorption due to such localized–extended or localized–localized transitions would be smaller than that of extended–extended transitions, due to the lower

density of states in the mobility gap region [31]. This fact may be related to the following observation: though E_{g1} and E_{g2} have only qualitative similarities to E_g^{Tauc} and E_g^{dir} (in the sense of E_{g1} being typically less than E_{g2}, particularly for the 400 °C films), it is notable that the TL oscillator corresponding to E_{g1} has a much smaller amplitude than the TLU oscillator corresponding to E_{g2} (as was mentioned above).

4. Results and discussion

We begin our discussion with the properties of the pure WO_3 thin films. XRD measurements indicated that the films annealed at both 250 and 400 °C were amorphous, in agreement with the earlier observations of amorphous structure in WO_3 films annealed at 400 °C made by sol–gel [32] and combined chemical vapor deposition sol–gel [33]

Table 2
Characteristics of the $(100 - x)$% WO_3–x% SiO_2 films annealed at 250 and 400 °C

Temp. (°C)	x%	d (nm)	d_{rough} (nm)	T (550 nm)	n (550 nm)	RMS (nm)
250	0.0	46 ± 2	13 ± 2	0.725	1.96 ± 0.02	14.7
	2.0	42 ± 1	20 ± 1	0.732	1.97 ± 0.03	11.1
	2.5	58 ± 2	0 ± 2	0.732	1.92 ± 0.01	10.7
	4.0	55 ± 2	0 ± 4	0.730	1.94 ± 0.01	9.7
	4.5	43 ± 1	20 ± 1	0.732	1.92 ± 0.03	19.2
400	0.0	38 ± 6	21 ± 5	0.748	1.94 ± 0.08	11.4
	2.0	60 ± 4	10 ± 5	0.755	1.86 ± 0.01	9.2
	2.5	61 ± 3	6 ± 6	0.811	1.73 ± 0.02	2.4
	4.0	58 ± 4	0 ± 9	0.815	1.74 ± 0.01	2.0
	4.5	58 ± 2	9 ± 3	0.815	1.73 ± 0.04	0.3

Transmittance T ($\lambda = 550$ nm) and root-mean-square (RMS) surface roughness are taken from the spectrophotometric and AFM measurements, respectively, while the film thickness d, surface roughness layer thickness d_{rough}, and refractive index n ($\lambda = 550$ nm) are derived from the best-fit results of the DTLU model.
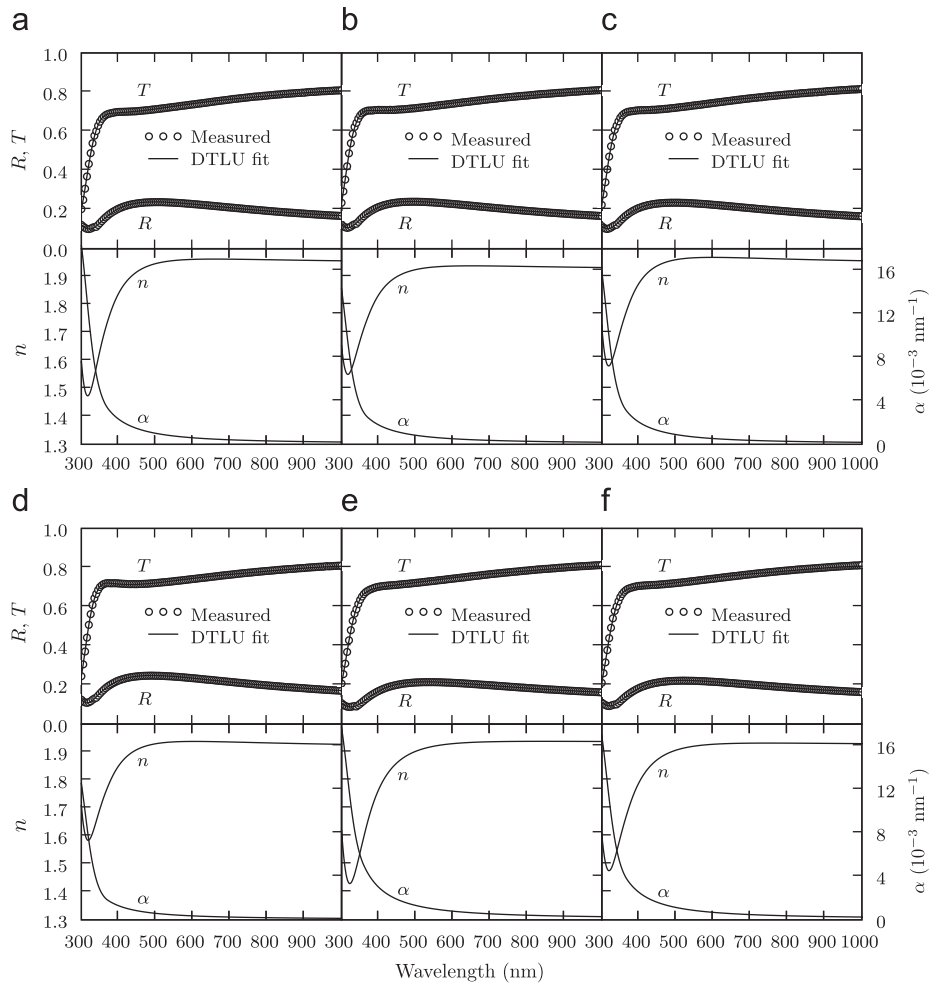

Fig. 2. Transmittance (T) and reflectance (R) spectra for the $(100 - x)$% WO_3–x% SiO_2 film–substrate systems annealed at 250 °C, together with the refractive index $n(\lambda)$ and absorption coefficient $\alpha(\lambda)$ for the film alone derived from fitting to the DTLU model. (a) 100% WO_3; (b) 99% WO_3 – 1% SiO_2; (c) 98% WO_3 – 2% SiO_2; (d) 96% WO_3 – 4% SiO_2; (e) 95.5% WO_3 – 4.5% SiO_2; (f) 95% WO_3 – 5% SiO_2.

methods. Our optical parameters, derived from the DTLU model and shown in Table 2, are also comparable to previous WO$_3$ studies. The refractive indices n ($\lambda = 550$ nm) $= 1.96 \pm 0.02$ (250 °C), 1.94 ± 0.08 (400 °C) are consistent with the literature, where values in the range 1.84–1.96 were seen for sol–gel-derived films heat treated between 100 and 500 °C [34–36]. We found Tauc and direct band gap energies $E_g^{Tauc} = 3.06 \pm 0.01$ eV (250 °C), 3.08 ± 0.02 eV (400 °C), $E_g^{dir} = 3.75 \pm 0.02$ eV (250 °C), 3.90 ± 0.04 eV (400 °C). Similar ranges of 3.0–3.4 eV for the Tauc, and 3.8–4.1 eV for the direct band gaps were seen in amorphous WO$_3$ films prepared using a variety of sputtering methods [25]. The total thickness ($d + d_{rough}$) is ~60 nm, and the root-mean-square (RMS) surface roughness, calculated from the AFM results and listed in Table 2, is 14.7 nm for 250 °C and 11.4 nm for 400 °C. The fitted surface roughness layers are in approximately the same size range, with $d_{rough} = 13 \pm 2$ nm (250 °C), 21 ± 5 nm (400 °C).

Turning now to the SiO$_2$-doped samples, we found that the films continued to be amorphous, and all total thicknesses fell in the range 50–70 nm, without any noticeable dependence on doping or temperature. The optical properties and surface morphology of the films, in contrast, do reveal significant changes with doping, particularly for the 400 °C films, as we describe in detail below. The transmittance and reflectance spectra of the film–substrate systems at selected dopings are shown in Fig. 2 (250 °C) and Fig. 3 (400 °C). Together with these measured values, the figures plot the best-fit T and R curves of the DTLU model, and the resulting refractive index $n(\lambda)$ and absorption coefficient $\alpha(\lambda)$ functions for the film alone, while Fig. 4 superimposes the film refractive indices for all dopings at each annealing temperature. The 5 μm × 5 μm AFM micrographs at various dopings are shown in Fig. 5 (250 °C) and Fig. 6 (400 °C).

For the 250 °C films, there is a slight shift in the optical and surface parameters between 4.0% and 4.5% doping. The Tauc band gap, which varies in the range 3.10–3.17 eV for 1.0–4.0% doping, drops to 2.93–3.00 eV for 4.5–5.0%. The RMS roughness, which decreases steadily from
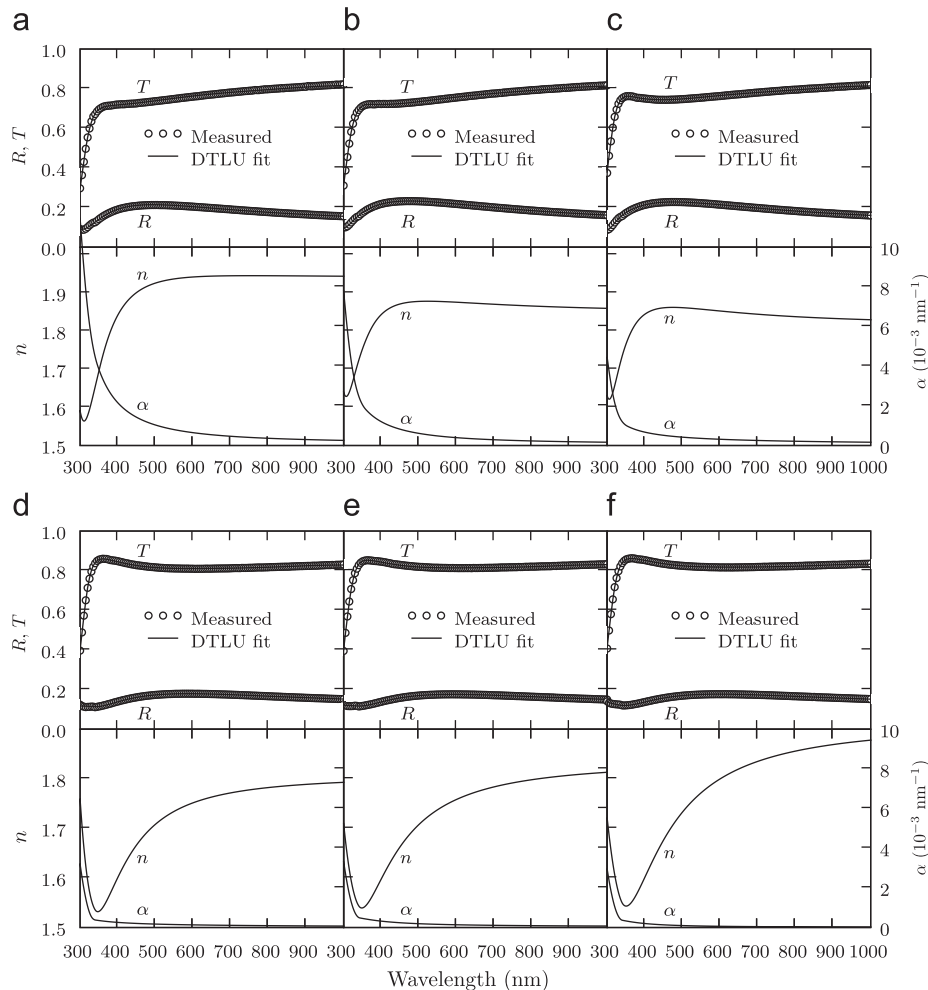

Fig. 3. Transmittance (T) and reflectance (R) spectra for the $(100 - x)$% WO$_3$–x% SiO$_2$ film–substrate systems annealed at 400 °C, together with the refractive index $n(\lambda)$ and absorption coefficient $\alpha(\lambda)$ for the film alone derived from fitting to the DTLU model. (a) 100% WO$_3$; (b)99% WO$_3$–1% SiO$_2$; (c) 98% WO$_3$–2% SiO$_2$; (d) 97.5% WO$_3$–2.5% SiO$_2$; (e) 96% WO$_3$–4% SiO$_2$; (f) 95% WO$_3$–5% SiO$_2$.

14.7 nm in the pure case to 9.7 nm at 4.0%, reverses its trend and jumps to 19.2 nm at 4.5%. On the other hand, the direct band gap remains roughly doping independent, staying within the range 3.72–3.82 eV, along with the transmittance T ($\lambda = 550$ nm)~0.725−0.732, and the refractive index n ($\lambda = 550$ nm)~1.91−1.97. The Urbach tail absorption, clearly seen in Fig. 2 as the exponential

contribution to $\alpha(\lambda)$ at longer wavelengths, is also approximately constant at all dopings.

The changes in the 400 °C films with doping are more dramatic. There are two distinct regimes, seen directly in Fig. 4(b) in the shape of the n curves: one for 0.0–2.0% doping, and the other for 2.5–5.0%. Both n (550 nm) and T (550 nm) change significantly between these two regimes.
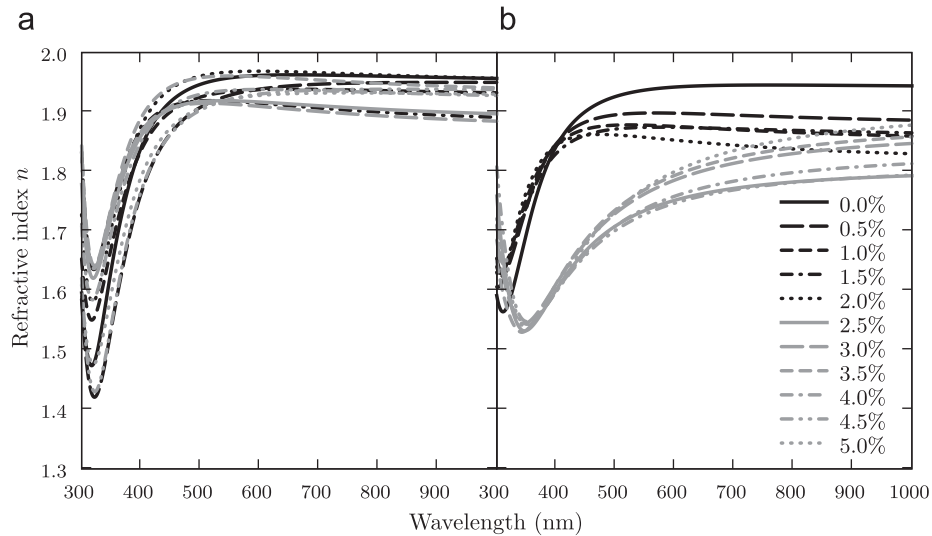

Fig. 4. Refractive indices $n(\lambda)$ for $(100-x)$% WO$_3$–x% SiO$_2$ thin films, $x = 0, 0.5, 1, \ldots, 5$%, derived from fitting to the DTLU model, for samples annealed at: (a) 250 °C; (b) 400 °C.
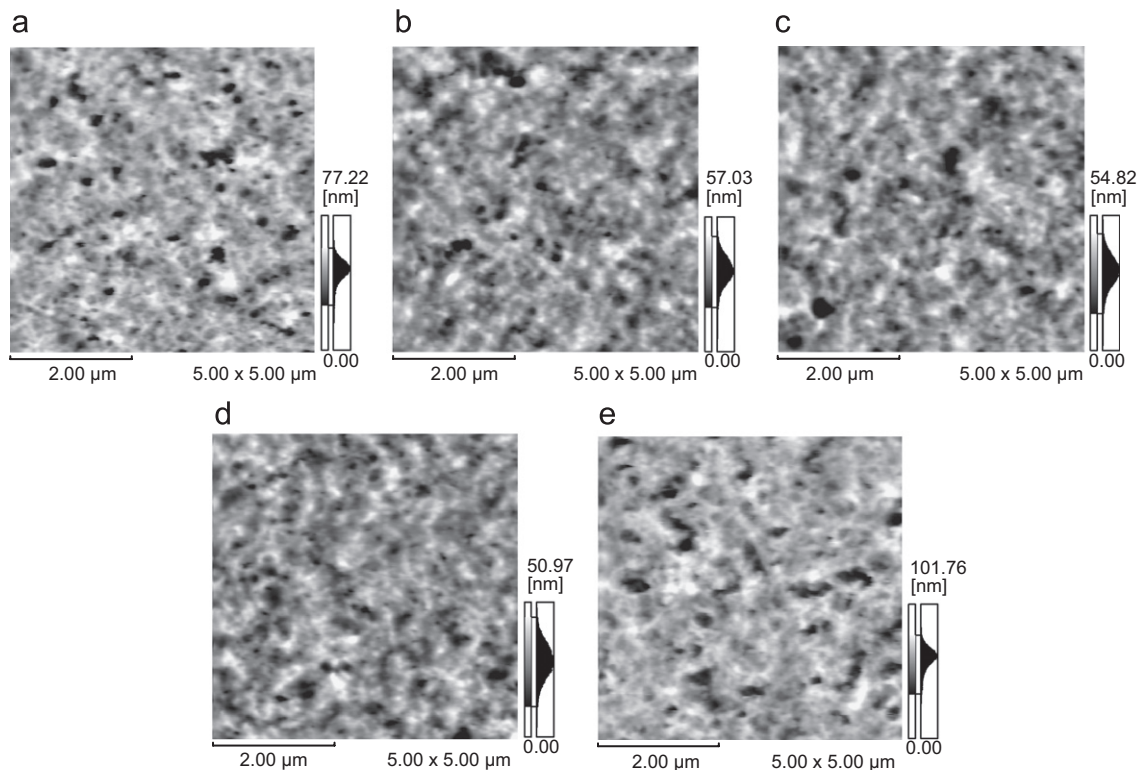

Fig. 5. AFM images of $(100-x)$% WO$_3$–x% SiO$_2$ thin films annealed at 250 °C for different compositions, depicting areas of dimension 5 μm × 5 μm. (a) $x = 0.0$%; (b) $x = 2.0$%; (c) $x = 2.5$%; (d) $x = 4.0$%; (e) $x = 4.5$%.

Fig. 6. AFM images of $(100 - x)\%$ WO$_3$–$x\%$ SiO$_2$ thin films annealed at 400 °C for different compositions, depicting areas of dimension $5\,\mu m \times 5\,\mu m$. (a) $x = 0.0\%$; (b) $x = 2.0\%$; (c) $x = 2.5\%$; (d) $x = 4.0\%$; (e) $x = 4.5\%$.
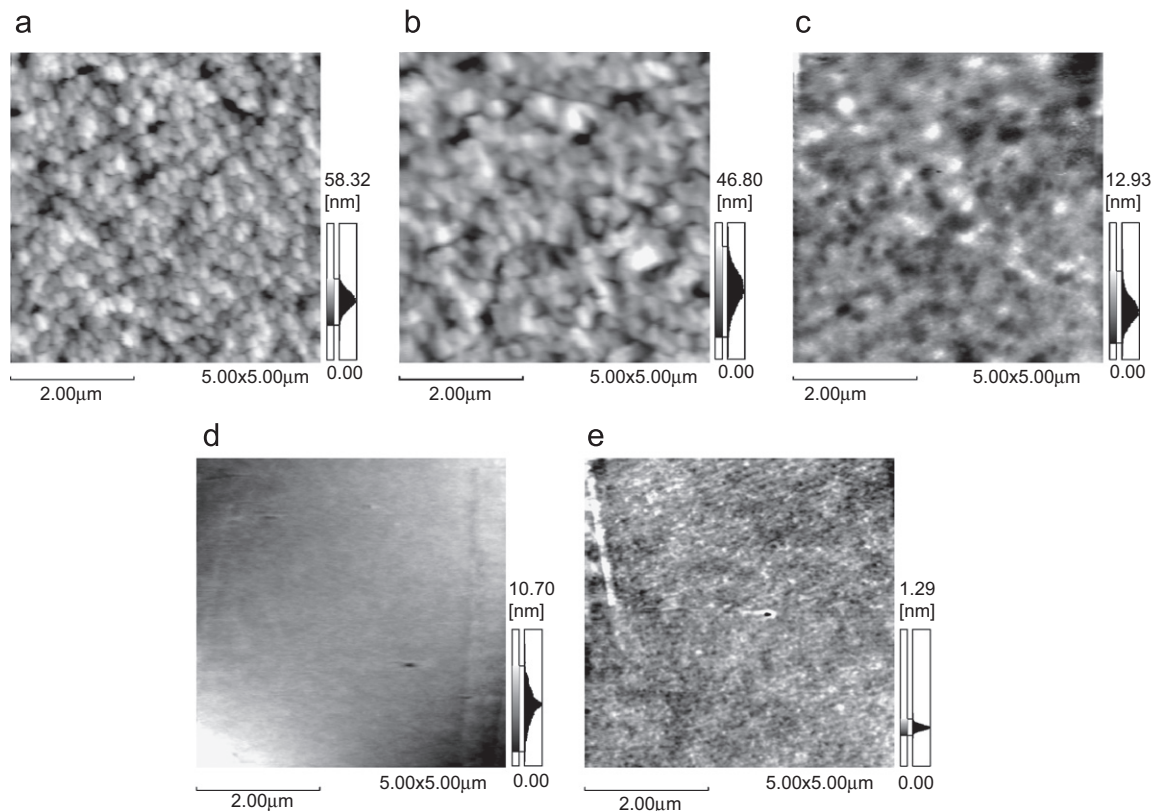
The former shifts from the range 1.86–1.94 for small dopings down to 1.73–1.77 for larger ones, while the latter increases from 0.744–0.749 to 0.811–0.821. The ranges of the band gap energies in the two regimes are similarly distinct. $E_g^{\text{Tauc}} \sim 3.08 - 3.32$ eV, $E_g^{\text{dir}} \sim 3.90 - 3.99$ eV for dopings through 2.0%, and these increase to $E_g^{\text{Tauc}} \sim 3.47 - 3.62$ eV, $E_g^{\text{dir}} \sim 4.03 - 4.06$ eV for 2.5% and above. Together with this change in band gap energies, the Urbach tails in $\alpha(\lambda)$, plotted in Fig. 3, become narrower at larger dopings. As for the surface morphology, RMS roughness drops from $\sim 9.2 - 11.4$ nm for 0.0–2.0% down to $\lesssim 2.4$ nm for 2.5–5.0%. This pronounced smoothing out of the surfaces can be observed directly in the AFM images of Fig. 6. Since corrections to T and R due to the surface roughness layer are typically very small, it can be difficult to extract reliable values of d_{rough} from the measured data. In several instances the fitting led to values of $d_{\text{rough}} = 0$ or large uncertainties. Despite these limitations, the overall trend of d_{rough} for the 400 °C case followed that of the RMS roughness, with larger d_{rough} values for 0.0–2.0%, and smaller ones for 2.5–5.0%.

5. Conclusions

We have shown that the optical characteristics of amorphous WO$_3$ and WO$_3$–SiO$_2$ composite sol–gel spin-coated thin films can be accurately modeled using a novel dielectric function consisting of two Tauc–Lorentz oscillators with an Urbach tail contribution. The model allows us to extract the evolution of the film optical parameters with doping, revealing interesting transitions at 4.0–4.5% and 2.0–2.5% SiO$_2$ dopings for films annealed at 250 °C and 400 °C, respectively. Coinciding with these transitions are changes in the surface morphology of the films. The model, which takes into account both multiple transitions and subgap absorption, is applicable to a more general class of materials, and is particularly suitable to extracting optical information from spectrophotometric and ellipsometric measurements of amorphous films.

References

[1] A. Agrawal, J.P. Cronin, R. Zhang, Sol. Energy Mater. Sol. Cells 31 (1993) 9.
[2] C.G. Granqvist, Handbook of Inorganic Electrochromic Materials, Elsevier Science, B.V., Amsterdam, The Netherlands, 1995.
[3] C.G. Granqvist, Sol. Energy Mater. Sol. Cells 60 (2000) 201.
[4] J. Livage, D. Ganguli, Sol. Energy Mater. Sol. Cells 68 (2001) 365.
[5] G.A. Niklasson, C.G. Granqvist, J. Mater. Chem. 17 (2007) 127.
[6] T. He, H.N. Yao, Res. Chem. Intermediates 30 (2004) 459.

[7] V. Wittwer, M. Datz, J. Ell, A. Georg, W. Graf, G. Walze, Sol. Energy Mater. Sol. Cells 84 (2004) 305.

[8] J. Tamaki, Sensor Lett. 3 (2005) 89.

[9] M. Klisch, J. Sol–Gel Sci. Technol. 12 (1998) 21.

[10] A.E. Aliev, H.W. Shin, Solid State Ionics 154–155 (2002) 425.

[11] X. Wang, G. Sakai, K. Shimanoe, N. Miura, N. Yamazoe, Sensors Actuators B: Chem. 45 (1997) 141.

[12] X.Q. Xu, H. Shen, X.Y. Xiong, Thin Solid Films 415 (2002) 290.

[13] N. Naseri, R. Azimirad, O. Akhavan, A.Z. Moshfegh, J. Phys. D: Appl. Phys. 40 (2007) 2089.

[14] R. Jin, H. Li, J.-F. Deng, J. Catal. 203 (2001) 75.

[15] F. Somma, G. Strukul, J. Catal. 227 (2004) 344.

[16] C. Martin, P. Malet, G. Solana, V. Rives, J. Phys. Chem. B 102 (1998) 2759.

[17] X. Xia, R. Jin, Y. He, J.-F. Deng, H. Li, Appl. Surf. Sci. 165 (2000) 255.

[18] G.E. Jellison Jr., F.A. Modine, Appl. Phys. Lett. 69 (1996) 371.

[19] A.S. Ferlauto, G.M. Ferreira, J.M. Pearce, C.R. Wronski, R.W. Collins, X. Deng, G. Ganguly, J. Appl. Phys. 92 (2002) 2424.

[20] D. Saygin Hinczewski, M. Hinczewski, F.Z. Tepehan, G.G. Tepehan, Sol. Energy Mater. Sol. Cells 87 (2005) 181.

[21] D. Saygin-Hinczewski, K. Koc, I. Sorar, M. Hinczewski, F.Z. Tepehan, G.G. Tepehan, Sol. Energy Mater. Sol. Cells 91 (2007) 1726.

[22] G.E. Jellison Jr., V.I. Merkulov, A.A. Puretzky, D.B. Geohegan, G. Eres, D.H. Lowndes, J.B. Caughman, Thin Solid Films 377–378 (2000) 68.

[23] D.A.G. Bruggeman, Ann. Phys. Leipzig 24 (1935) 636.

[24] J. Tauc, in: F. Abelès (Ed.), Optical Properties of Solids, Elsevier, Amsterdam, 1970, p. 299.

[25] J. Kleperis, J. Zubkāns, A. Lūsis, Proc. SPIE 2968 (1997) 186.

[26] H. Chen, W.Z. Shen, Eur. Phys. J B 43 (2005) 503.

[27] B. von Blanckenhagen, D. Tonova, J. Ullmann, Appl. Opt. 41 (2002) 3137.

[28] Y.J. Choi, N.V. Nguyen, C.A. Richter, J.R. Ehrstein, B.H. Lee, J.C. Lee, Appl. Phys. Lett. 80 (2002) 1249.

[29] Z.G. Hu, J.H. Ma, Z.M. Huang, Y.N. Wu, G.S. Wang, J.H. Chu, Appl. Phys. Lett. 83 (2003) 3686.

[30] J.J. Moré, B.S. Garbow, K.E. Hillstrom, User guide for MINPACK-1, Argonne National Laboratory Report ANL-80-74, Argonne, IL, 1980.

[31] S.R. Elliott, Physics of Amorphous Materials, Longman, London, 1984, p. 236.

[32] C. Cantalini, M.Z. Atashbar, Y. Li, M.K. Ghantasala, S. Santucci, W. Wlodarski, M. Passacantando, J. Vac. Sci. Technol. A 17 (1999) 1873.

[33] M. Basato, E. Brescacin, E. Tondello, Chem. Vapor Deposition 7 (2001) 219.

[34] N. Ozer, Thin Solid Films 304 (1997) 310.

[35] M. Deepa, R. Sharma, A. Basu, S.A. Agnihotry, Electrochim. Acta 50 (2005) 3545.

[36] M. Deepa, T.K. Saxena, D.P. Singh, K.N. Sood, S.A. Agnihotry, Electrochim. Acta 51 (2006) 1974.